Chemical Engineering Journal 442 (2022) 136276

Contents lists available at ScienceDirect

Chemical Engineering Journal

journal homepage: www.elsevier.com/locate/cej

Seignette salt induced defects in Zr-MOFs for boosted Pb(II) adsorption: universal strategy and mechanism insight

Yu-Hang Li [a,b], Chong-Chen Wang [a,b,*], Xu Zeng [a,b], Xue-Zi Sun [a,b], Chen Zhao [a,b], Huifen Fu [a,b], Peng Wang [a,b]

[a] Beijing Key Laboratory of Functional Materials for Building Structure and Environment Remediation, School of Environment and Energy Engineering, Beijing University of Civil Engineering and Architecture, Beijing 100044, China
[b] Beijing Energy Conservation & Sustainable Urban and Rural Development Provincial and Ministry Co-construction Collaboration Innovation Center, Beijing University of Civil Engineering and Architecture, Beijing 100044, China

ARTICLE INFO

Keywords:
Zr-MOFs
Seignette salt
Hierarchical pores
Pb(II) adsorption
DFT calculation

ABSTRACT

Within this work, a green and facile approach was proposed to modulate NH_2-UiO-66 for purpose of obtaining SS-NH_2-UiO-66-X ("X" implied the dosage of used SS) using seignette salt (SS). The generation of abundant vacancies with the formation of hierarchical pores boosted their sorption performance for lead (Pb(II)), which strengthened the mass transfer of Pb(II) in SS-NH_2-UiO-66-X interior. Particularly, the optimal SS-NH_2-UiO-66-5 exhibited good adsorption capacity toward Pb(II) (186.14 mg g^{-1}) and fast diffusion rate (32.1 mg g^{-1}·$min^{0.5}$) at 25 °C and initial pH = 5.46, which were about 34.2 and 66.9 times higher than those of the pristine NH_2-UiO-66, respectively. SS-NH_2-UiO-66-5 could selectively capture the Pb(II) from simulated wastewater containing different co-existing ions. The mechanism was proposed that the defect sites played a significant role in boosting the Pb(II) capture performance, which was further affirmed by X-ray absorption spectroscopy (XAS) and X-ray photoelectron spectra (XPS). The density functional theory calculations (DFT calculations) illustrated that the hierarchical pores and rich vacancies enhanced the Pb(II) mobility toward the adsorption active sites and reduced the adsorption energy between SS-NH_2-UiO-66-X and Pb(II). This defect engineering approach could be introduced to modulate other Zr-MOFs like MOF-801, UiO-66 and MOF-808, which presented a general strategy to fabricate defective Zr-MOFs for the boosted adsorption performance toward pollutants removal from wastewater.

1. Introduction

Metal-organic frameworks (MOFs), constructed from metal/cluster and organic linkers, were highly porous crystalline materials, which attracted increasing attentions from different research fields [1–5]. Among the large family, Zr-MOFs, with the merits of the high coordination number, strong chemical stability, huge specific surface area and low toxicity [6–8], had propelled Zr-MOFs into the application of adsorption for removing various pollutants from wastewater [9]. Different from the traditional adsorbents like activated carbon, zeolite, and molecular sieve, Zr-MOFs displayed some advantages like highly tunable structures, compositions, and pore sizes [10–12]. The pore sizes of most previously reported Zr-MOFs were limited to a specific micropore range with pore diameter less than 2 nm, which might decrease the mass transfer rates, inhibit the pollutant diffusion from substrates to adsorption sites [13,14]. Thus, many researchers devoted to developing effective approaches to modify different Zr-MOFs for the enhancement of sorption capacity.

Isoreticular expansion was an approach for expanding pore size and enlarging surface area [15]. Wang et al. adopted the isoreticular expansion strategy to obtain series Zr-MOFs from NU-1101 to NU-1104, with the increasing pore size of 24.3, 25.3, 27.9 and 28.7 Å, respectively [16]. Defect engineering was an effective strategy to boost the adsorption performance toward pollutants via constructing extra bonding sites [17,18]. In recent years, increasing studies began to pay great attention in fabricating hierarchical porous Zr-MOFs via modulating and templating (Fig. S1), which could enhance the pore volume and expose active sites [11,19]. For instance, Li et al. used different fatty acids as

* Corresponding author at: Beijing Key Laboratory of Functional Materials for Building Structure and Environment Remediation, School of Environment and Energy Engineering, Beijing University of Civil Engineering and Architecture, Beijing 100044, China.
E-mail address: wangchongchen@bucea.edu.cn (C.-C. Wang).

https://doi.org/10.1016/j.cej.2022.136276
Received 21 February 2022; Received in revised form 4 April 2022; Accepted 5 April 2022
Available online 9 April 2022

modulators/templates to fabricate HP-UiO-66-XA adsorbents with tunable mesopores and different diameters for phosphate removal [20]. In Li's work, the pore volumes of mesopores were 38.8%, 41.7% and 64.3% for HP-UiO-66(Zr)-FA, HP-UiO-66(Zr)-BA and HP-UiO-66(Zr)-OA, respectively, which displayed increasing phosphate sorption capacities from 37.7 mg g^{-1} to 186.6 mg g^{-1}. Cai et al. [21] and Pei et al. [22] also prepared HP-Zr-MOFs via the modulation of sodium acetate and sodium benzoate to achieve the enhancement of adsorption performances toward organic dyes and Dy^{3+}, respectively. In all, the modulation approaches using the monocarboxylic acids/salts mainly demonstrated two aspects: (i) enlarging pores size and pore volume to facilitate targets into the frameworks further increased mass transfer rates; (ii) exposing some sorption sites (e.g., unsaturated coordination centers) via the absence of linkers or clusters. In fact, the boosted sorption performances were primarily contributed to the increasing sorption sites. However, few reports concerning vacancies enriched defect in MOFs via tuning their structure were available with the purpose of providing more sorption sites for pollutants removal.

Herein, a facile and green post-modification strategy was presented by using seignette salt with different concentration to modulate different Zr-MOFs (like NH_2-UiO-66, UiO-66, MOF-801 and MOF-808) for obtaining hierarchical porous adsorbents with abundant vacancies to accomplish effective and selective Pb(II) adsorptive removal. With the development of smelting industry and the substandard discharge of smelting wastewater, the wastewater containing Pb(II) was discharged to nature environment [23,24]. The Pb(II) exerted significant risks to human health due to that it was inherently toxic to brain tissue, the nervous system, and the reproductive system [25]. However, the adsorption capacities of the pristine Zr-MOFs toward Pb(II) were poor due to that: (i) the limited windows of Zr-MOFs (e.g., MOF-801: ca. 4.8 Å, UiO-66: ca. 6 Å, MOF-808: ca. 18.4 Å [26,27]) decreased the diffusion rate of Pb(II) into the frameworks; (ii) Zr-MOFs lacked abundant sorption sites for Pb(II) uptake. The seignette salt was selected as the modulator to finely tune NH_2-UiO-66, considering that (i) it could be used as a flavoring agent with non-toxic and harmless properties [28] and (ii) it was regarded as a good chelating agent to form soluble complex with Zr(IV) in aqueous solution [29]. In the whole modulation process, the rich vacancies (the unsaturated coordination oxygen groups) will be exposed, and the absence of linkers resulted in the formation of hierarchical pores, which provided more opportunities to form both Pb-O bonds and Pb-N bonds. Up to now, few studies were undertaken to explore the defective Zr-MOFs for boosting its adsorption performances toward cationic heavy metal pollutants like Pb(II). This study could provide general approach and intensive mechanism insights into the defective Zr-MOFs for environmental applications, thus, affording a green and promising solution for effective lead removal from smelting wastewater.

2. Materials and methods

2.1. Chemicals

Zirconium (IV) chloride ($ZrCl_4$, purity ≥ 99%), benzene-1,4-dicarboxylic acid (H_2BDC, purity ≥ 99%), 2-aminoterephthalic acid (H_2BDC-NH_2, purity ≥ 99%), 1,3,5-benzenetricarboxylic acid (H_3BTC, purity ≥ 99%), fumaric acid (H_2FA, purity ≥ 99%), zirconium dichloride oxide octahydrate ($ZrOCl_2{\cdot}8H_2O$, purity ≥ 99%) were brought from J&K company. Dimethylformamide (DMF), methanol (MeOH), acetic acid (purity ≥ 99.5%) were obtained from Tianjin Fu Chen Chemical Co., Ltd. (China). Seignette salt (SS, $KNaC_4H_4O_6{\cdot}4H_2O$, analytically pure) was brought from Sinopharm Chemical Reagent Co., Ltd. (China). Lead nitrate ($Pb(NO_3)_2$, analytically pure) was brought from Beijing Chemical Reagent Co., Ltd. (China). All chemicals were directly used without further purification.

2.2. Synthesis of defective SS-Zr-MOFs-X

The pristine MOF-801, UiO-66, NH_2-UiO-66 and MOF-808 were synthesized following the previous methods [27,30,31] listed in the Supporting Information (SI), Section S1. In the main text, the preparation of SS-NH_2-UiO-66-X was selected to be described. Briefly, 100.0 mg as-prepared NH_2-UiO-66 and seignette salt (SS) with different dosage (1.0 mmol, 3.0 mmol, 5.0 mmol and 7.0 mmol) were added to 50.0 mL deionized water in the glass beaker. Then, the mixture was heated at 60 °C for 10.0 h. Finally, the obtained solid (like SS-NH_2-UiO-66-5, the number "5″ implied the added SS was 5.0 mmol) washed with ultra-pure water three times, and dried at 60 °C for 12.0 h. The fabrication methods of SS-MOF-801-X, SS-UiO-66-X and SS-MOF-808-X were identical to that of SS-NH_2-UiO-66-X.

2.3. Characterizations

The physicochemical properties of the as-prepared materials were characterized by the powder X-ray diffraction (PXRD), Fourier transform infrared spectra (FTIR), scanning electron microscope (SEM), high resolution transmission electron microscopy (HR-TEM), X-ray photoelectron spectra (XPS), X-ray absorption spectroscopy (XAS), thermogravimetric analyses (TGA), differential scanning calorimetry (DSC), elemental analyses (EA), Brunauer-Emmett-Teller (BET), electron paramagnetic resonance (EPR). The detail information of the characterization techniques as well as density functional theory (DFT) calculations were presented in the SI, Section S4.

2.4. Batch adsorption experiments

The Pb(II) adsorption experiments were conducted using $Pb(NO_3)_2$ as the model pollutant. The initial pH of the obtained Pb(II) aqueous solution was 5.46, and the required pH of the solution was adjusted by HCl or NaOH solutions with suitable concentration. During the adsorption procedure, each 2.5 mL solution was filtered using 0.22 μm PTFE membrane at specified time intervals to determine the residual Pb (II) concentrations by ICP-OES (ICP-5000, Focused Photonics Inc., China). The adsorption capacities of NH_2-UiO-66 and series SS-NH_2-UiO-66-X toward Pb(II) were calculated by Eq. S1, Section S2.

For adsorption kinetic experiments, 20.0 mg of different adsorbents were added into a 150.0 mL Pb(II) solution with an initial concentration of 15.0 mg L^{-1}. The matrix was shaken with a speed of 170.0 rpm up to 90.0 min to accomplish adsorption–desorption equilibrium at 25 °C and pH = 5.46. The kinetic curves were fitted with the pseudo-first-order model, pseudo-second-order model along with Weber-Morris intraparticle diffusion model (SI, Section S2), respectively. The adsorption kinetic experiments of the optimal adsorbent were tested adopting Pb(II) solutions with different initial concentrations (5.0, 15.0, 30.0 and 40.0 mg L^{-1}). To acquire thermodynamic parameters and the adsorption isotherms of the optimal adsorbent, the corresponding adsorption experiments were conducted under 15 °C, 25 °C and 35 °C at a stirring speed of 170.0 rpm for 120.0 min. The isotherm curves were fitted with Langmuir, Freundlich and Dubinin-Radushkevich (D-R) models, respectively (SI, Section S2).

2.5. Cyclic experiments

20.0 mg of SS-NH_2-UiO-66-5 as the optimal adsorbent was added into a 100.0 mL Pb(II) solution with 5.0 mg L^{-1}, and the mixture solution was shaken up to 90.0 min. To check the regeneration ability, 10.0 mg of the exhausted SS-NH_2-UiO-66-5 was regenerated by washing with 10.0 mL of HCl solution (pH = 2.0) at 25 °C with the aid of stirring for 1.0 min. Then, the regenerated adsorbents were washed by ultra-pure water four times and dried at 60 °C for 6.0 h before the next cycle. All adsorption experiments were conducted parallelly three times to ensure good reproducibility.

2.6. Column experiments

The fixed-bed column experiments were performed in the solid phase extraction (SPE) column (the setup picture was provided in Fig. S11a). 50.0 mg adsorbents (SS-NH_2-UiO-66-5, NH_2-UiO-66, zeolite (natural zeolite, 1.0 mm – 2.0 mm), resin (D301, 0.5 mm – 1.5 mm) and molecular sieve (4A, 3.0 mm – 5.0 mm)) were packed into the empty SPE column. The Pb(II) solution with the concentration of 2.0 mg L^{-1} flowed through the as-prepared column with a constant flow rate (6.0 mL min^{-1}) with the aid of vacuum pump.

After breaking through the maximum adsorption capacity, the HCl solution (pH = 2.0) was pumped through the SPE column for desorption. During the adsorption and desorption processes, 5.0 mL sample was collected to determine the Pb(II) concentration at regular intervals by ICP-OES.

3. Results and discussion

3.1. Characterizations of the defective SS-NH_2-UiO-66-X

The powder X-ray diffraction (PXRD) patterns of the as-prepared NH_2-UiO-66 and series SS-NH_2-UiO-66-X were identical to that of NH_2-UiO-66 simulated from its single crystal data (CCDC: 1507786), as depicted in Fig. 1a, implying that their structures were maintained well after defect introduction. However, it was worth noting that the Zr-O lattice planes (1 1 1) at 7.32° was gradually damaged [32] with the increasing seignette salt concentration, indicating that the defect content gradually increased. The scanning electron microscope (SEM) images (Fig. 1b–f) demonstrated that the pristine NH_2-UiO-66 and series SS-NH_2-UiO-66-X displayed octahedral morphology with particle sizes ranging from 500 nm to 700 nm. Moreover, the main peaks in the Fourier transform infrared spectra (FTIR) of series SS-NH_2-UiO-66-X were retained compared to those of NH_2-UiO-66, further affirming the pristine structure of defective SS-NH_2-UiO-66-X was well maintained (Fig. S2). The N_2 adsorption–desorption isotherms as well as the pore size distribution were conducted to investigate the influence of seignette salt on the pore dimensions of SS-NH_2-UiO-66-X. As depicted in Fig. S3, the pristine NH_2-UiO-66 displayed a type I isotherm, indicating the typical of a microporous structure. By contrast, all SS-NH_2-UiO-66-X exhibited typical type Ⅳ isotherms with slight adsorption–desorption hysteresis in $0.8 < P/P_0 < 1.0$, indicating that there were additional mesopores in the adsorbents [33,34]. The existence of additional mesopores in the defective SS-NH_2-UiO-66-X was confirmed by the pore size distribution plots (Fig. 2a). More excitingly, all SS-NH_2-UiO-66-X exhibited mesopores (26.0 – 50.0 nm) and macropores (50.0 – 120.0 nm), which were different from that of NH_2-UiO-66 (2.0 – 4.0 nm). Combined with Table S1, the effect of seignette salt concentration toward the percentage of mesopore volume displayed the saddle-shaped curve, in which the pore volume of mesopores increased from 39.67% to 70.91% with the dosage of the seignette salt increasing from 1.0 to 5.0 mmol. As shown in Fig. 1g–j, the high-resolution transmission electron microscopy (HR-TEM) directly demonstrated that the local magnification of SS-NH_2-UiO-66-5 (Fig. 1j) displayed obvious defect compared to NH_2-UiO-66 (Fig. 1h). The *d* spacings of 2.3 Å corresponded to the (1 1 1) planes of NH_2-UiO-66 [35], indicating that SS-NH_2-UiO-66-5 kept good crystallinity after the modulation process.

The generation of hierarchical pores was mainly attributed to the linkers or clusters missing [13]. Thermogravimetric analyses (TGA), electron paramagnetic resonance (EPR), X-ray photoelectron spectra (XPS) and CHNO elemental analyses (EA) were conducted to explain the effects of seignette salt with different dosages on the structural characteristics of the pristine NH_2-UiO-66 and the defective NH_2-UiO-66. The TGA was adopted to qualitatively clarify the thermal decomposition properties of the samples [36,37]. As shown in Fig. 2b and c, two weight loss regions could be detected in the TGA curves with the increasing temperature: (i) the physically adsorbed and the lattice water (50 °C –

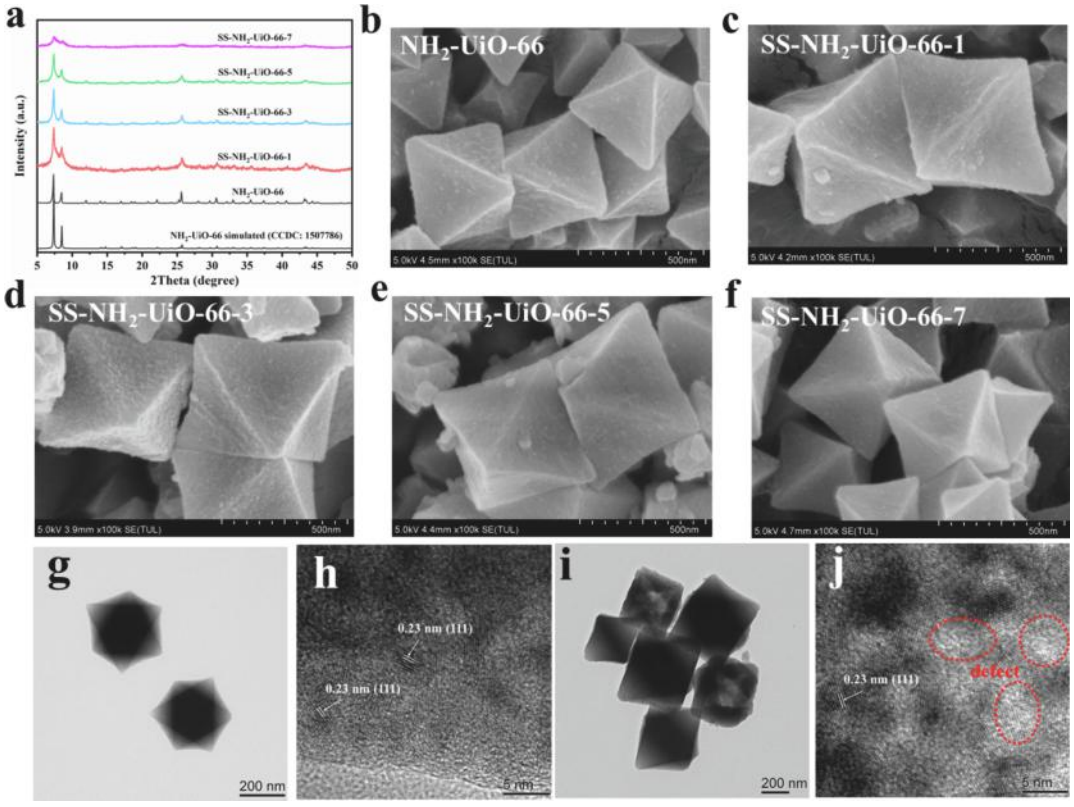

Fig. 1. (a) The PXRD patterns of NH_2-UiO-66 and series SS-NH_2-UiO-66-X, and (b-f) their corresponding SEM images. HR-TEM images of (g, h) NH_2-UiO-66 and (i, j) SS-NH_2-UiO-66-5.

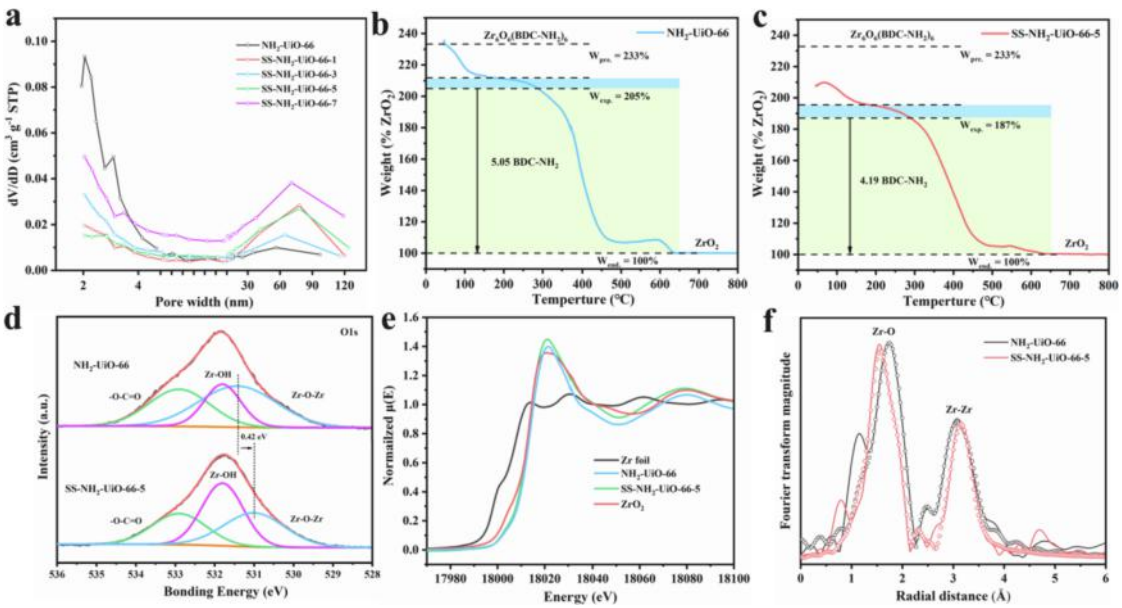

Fig. 2. (a) The pore size distributions curves (the BJH desorption model) of NH_2-UiO-66 and series SS-NH_2-UiO-66-X. TGA curves of (b) NH_2-UiO-66 and (c) SS-NH_2-UiO-66-5. (d) The spectra of O 1s of pristine NH_2-UiO-66 and SS-NH_2-UiO-66-5. (e) XANES and (f) EXAFS spectra of the Zr K-edge in NH_2-UiO-66 and SS-NH_2-UiO-66-5. The experimental and calculated curves were plotted as black/red lines and black/red open circles, respectively.

290 °C) [38]; (ii) the linkers (BDC-NH_2) decomposition (300 °C – 640 °C) followed by an noticeable exothermic peak in the DSC plot (Fig. S4a and b) [39]. The calculated weight losses of ligands in NH_2-UiO-66 and SS-NH_2-UiO-66-5 were 105.0% and 87.0% in range of 300 °C – 640 °C, in which the coordination numbers of Zr-O cluster in NH_2-UiO-66 and SS-NH_2-UiO-66-5 were calculated as 5.05 and 4.19, respectively (the detailed calculation about the TGA results was given in SI, Section S2). Theoretically, each $[Zr_6O_4(OH)_4]$ cluster in NH_2-UiO-66 was coordinated and stabilized by at least six BDC-NH_2 linkers [20], indicating that the $[Zr_6O_4(OH)_4]$ cluster in SS-NH_2-UiO-66-5 were not easy to miss completely. The decrease of characteristic element N in the EA results (Table S2) also confirmed the miss of the partial linkers after the modulation process. For instance, the mean miss number of BDC-NH_2 linker from the results of EA was 1.0 which was in good agreement with the difference between NH_2-UiO-66 and SS-NH_2-UiO-66-5 as well as the average miss number of TGA (0.86). As depicted in Fig. S5, the EPR spectrum of the NH_2-UiO-66 displayed a peak at $g = 2.004$ [40,41], which might be attributed to the original oxygen vacancies upon the addition of acetic acid in the synthesis process. After the modulation process, the spectrum displayed a noticeable peak with the same g value, indicating that an increasing amount of uncoordinated and defective Zr (IV) centers in the frameworks existed. Moreover, the defects content increased considerably with the increasing seignette salt concentration. Due to the existence of rich uncoordinated Zr(IV) centers and –OH group compensation (–OH) model [20], the Zr-OH peak (531.8 eV) [42] areas in the O 1 s signal (Fig. 2d) exhibited a significant increase from 22.1% of the pristine NH_2-UiO-66 to 40.7% of SS-NH_2-UiO-66-5. In addition, the XPS, EA, X-ray absorption near-edge spectroscopy (XANES) and extended X-ray absorption fine structure (EXAFS) results affirmed that the seignette salt led to partial missing of Zr on the Zr-O clusters in NH_2-UiO-66 without destroying the cluster framework further confirming the rich Zr vacancies in the SS-NH_2-UiO-66-5, as depicted in Fig. 3 (structure diagram of Zr-O cluster). In the O 1s signal (Fig. 2d), a blue shift of 0.42 eV happened to the binding energy of Zr-O-Zr peak of NH_2-UiO-66 and SS-NH_2-UiO-66-5 with the peak areas decreasing from 45.3% to 33.4%, indicating that partial Zr-O-Zr bonds were broken during the defect fabrication process [43]. As shown in Table S2, the Zr element mass percentages of all adsorbents did not change significantly even though there was a large amount of ligand loss. It was observed from the TGA results that it was not easy to cause the missing Zr-O cluster in the modulation process. If the theoretical ligand weight loss was supplemented, the Zr element mass percentages of SS-NH_2-UiO-66-X (e.g., the Zr element mass percentage of SS-NH_2-UiO-66-5 was 31.4%) will decrease compared to that of NH_2-UiO-66 (34.9%). The uncoordinated oxygen required to combine with hydrogen to maintain a stable state, explaining why the Zr-OH peak areas (Fig. 2d) of SS-NH_2-UiO-66-5 exhibited a noticeable increase in comparison with that of NH_2-UiO-66. The XANES spectra (Figs. 2e and S6) illustrated that the Zr oxidation state did not significantly change after modulation by seignette salt. However, it was non-negligible that the intensity of white line (first resonance after the edge) increased after the modulation process. According to previous reports, the intensity decline of the white line might be attributed to the loss of BDC-NH_2 in the outermost coordination shell around Zr centers [39,44]. Thus, the intensity increase of the white line may be considered to the loss of Zr on the Zr-O cluster. The EXAFS spectra displayed the local coordination surrounding of the Zr centers, in which the two primary peaks at 1.7 and 3.1 Å could be ascribed to the Zr-O and Zr-Zr, respectively (Fig. 2f, S7 and Tables S3) [39]. It was obviously observed that significant shifts happened to the Zr-O and Zr-Zr peak positions of NH_2-UiO-66 and SS-NH_2-UiO-66-5. The blue shift of the Zr-O peak happened in NH_2-UiO-66 and SS-NH_2-UiO-66-5, which could be attributed to the formation of oxygen vacancy and the introduction of OH^-/H_2O into the framework [41]. The change of Zr-Zr peak width and the decrease of Zr-Zr coordination number were attributed to the missing Zr in the Zr-O cluster, which agreed well the results of TGA, EA and XPS. The introduction of seignette salt not only resulted in the formation of hierarchical pores but also generated more active sites (Zr vacancies), which was different from the previous approaches [13,20,21,43] (Fig. S1). Combining the above-mentioned results, the Zr atoms in the pristine NH_2-UiO-66 were coordinately saturated with BDC-NH_2 ligands to build uniform micropores (Fig. 3a). During the post-modification process, the introduced seignette salt would take away partial Zr atoms in the prefect NH_2-UiO-66 via chelating interactions. The missing zirconium could subsequently cause the loss of the linkers, further resulting in the generation of oxygen vacancy and hierarchical pores. Meanwhile, the missing Zr atoms on the Zr-O cluster could yield the uncoordinated oxygen (Zr vacancies), as described in Fig. 3b. Considering the above-mentioned results, it was affirmed that SS-NH_2-

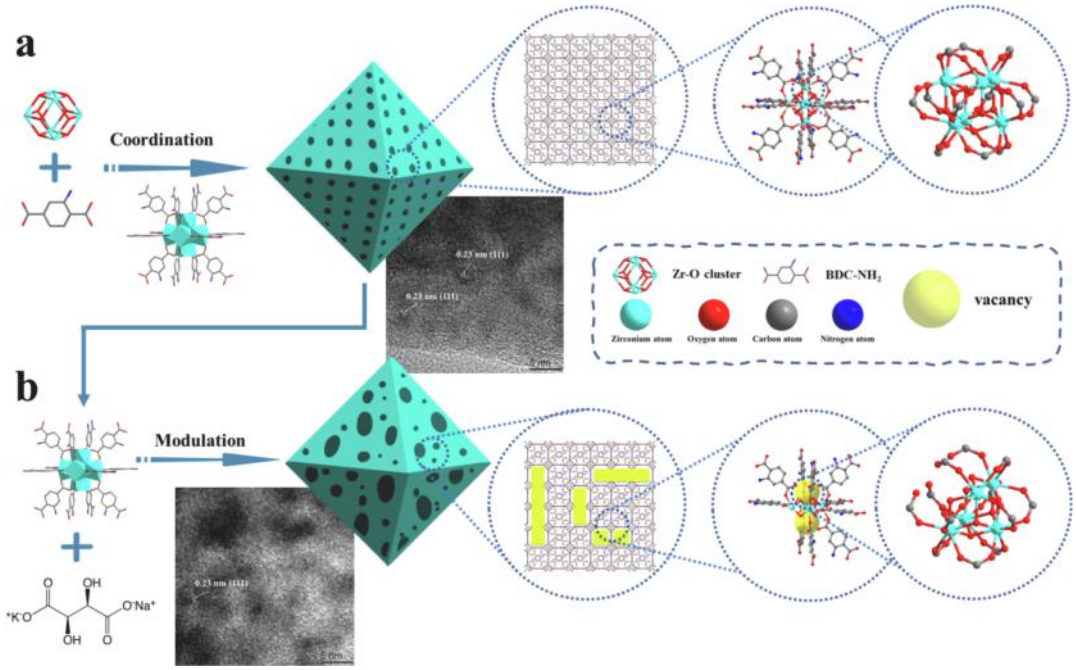

Fig. 3. The Schematic illustration for (a) pristine NH_2-UiO-66 and (b) defective SS-NH_2-UiO-66-X.

UiO-66-X with hierarchical pores and abundant vacancies (Zr vacancies and oxygen vacancies) were successfully synthesized.

3.2. Lead adsorption performance of the SS-NH_2-UiO-66-X

The adsorption capacity and adsorption rate were the two significant factors for efficient removal of pollutants from water solution. All the SS-NH_2-UiO-66-X demonstrated superior adsorption capacity and rate toward Pb(II) to the pristine NH_2-UiO-66 (Fig. 4a), in which the SS-NH_2-UiO-66-5 was considered as the optimal adsorbent due to the highest adsorption rate and adsorption capacity. The adsorption kinetic curves fitted better with pseudo-second-order model ($R^2 > 0.99$) than pseudo-first-order model, implying that the adsorption process was dominated by chemical adsorption (Table S4) [45]. The Weber-Morris intraparticle diffusion model was adopted to explore the intraparticle diffusion process. As described in Fig. 4b and Table S5, compared with pristine NH_2-UiO-66 (k_1, 0.48 mg g^{-1} $min^{0.5}$), the optimal adsorbent SS-NH_2-UiO-66-5 exhibited rapid liquid film diffusion rate (k_1, 32.09 mg g^{-1} $min^{0.5}$), due to the presence of uncoordinated oxygen and the negative surface zeta potential (Fig. S8a). It was worth noting that the presence of abundant uncoordinated oxygen could perfectly explain why the zeta potential of SS-NH_2-UiO-66-5 decreased quicker at high pH than that of NH_2-UiO-66. This conclusion was also agreed well with the results of EA (Table S2) and XPS. Moreover, the internal diffusion rate (k_2) displayed the saddle-shaped curve with the increasing seignette salt dosage, which was consistent with the change of mesopore volume percentage. As well, the internal diffusion rate followed the order SS-NH_2-UiO-66-5 (6.60 mg g^{-1} $min^{0.5}$) > SS-NH_2-UiO-66–3 (5.69 mg g^{-1} $min^{0.5}$) > SS-NH_2-UiO-66-7 (3.64 mg g^{-1} $min^{0.5}$) > SS-NH_2-UiO-66-1 (2.58 mg g^{-1} $min^{0.5}$) > NH_2-UiO-66 (0.21 mg g^{-1} $min^{0.5}$). Due to the presence of the large pore dimensions and rich vacancies, the time required to accomplish the Pb(II) adsorption–desorption equilibrium was cut from 90.0 min (NH_2-UiO-66) to 30.0 min (SS-NH_2-UiO-66-X), implying that the formed hierarchical pores could significantly boost the mass transport of Pb(II), and the uncoordinated oxygen offered more active sites within SS-NH_2-UiO-66-X. As described in Fig. S9, SS-NH_2-UiO-66-5 could reach adsorption equilibrium within 60.0 min under both low-concentration (5.0 mg L^{-1}) and high-concentration (40.0 mg L^{-1}) Pb(II) solution. And it could demonstrate 100% removal efficiency within 15.0 min for 5.0 mg L^{-1} Pb (II) solution. The adsorption kinetic curves still fitted well with pseudo-second-order model (Fig. S9 and Table S6). Meanwhile, because seignette salt induced the missing Zr atoms on the Zr-O cluster, and further led the loss of the ligands in frameworks. Thus, other Zr-MOFs like UiO-66, MOF-801 and MOF-808 assembled from H_2BDC, H_2FA and H_3BTC were selected to be treated by SS via the identical modulation strategy to boost their adsorption performances, as seen in Fig. S10.

Fig. 4c demonstrated the Pb(II) adsorption capacities of SS-NH_2-UiO-66-5 as a function of Pb(II) concentration under different temperature (15 °C, 25 °C and 35 °C). The isotherms fitted better with Langmuir model ($R^2 > 0.99$) than Freundlich and D-R models (Freundlich $R^2 > 0.93$, D-R $R^2 > 0.87$), demonstrating that the sorption process originated from a monolayer adsorption (Table S7) [46]. As revealed by the adsorption isotherm experiments, the maximum adsorption capacity (q_{max}) of SS-NH_2-UiO-66-5 was 186.14 mg g^{-1} at 25 °C within 90.0 min, which was about 34.2 times higher than that of pristine NH_2-UiO-66 (5.44 mg g^{-1}). Significantly, the adsorption efficiency of SS-NH_2-UiO-66-5 was higher than those of most other types of adsorbents reported previously like Chitosan nanofibrils [47], PBC@SiO_2-NH_2 [48], Palm shell activated carbon [49]. In addition, the enhancement of both adsorption rate and adsorption capacity of SS-NH_2-UiO-66-5 was better than those of the counterpart adsorbents like UiO-66-PTC and UiO-66-RSA (Table S9) [50,51]. Further, according to the Langmuir model, all the standard free energy change (ΔG^0), enthalpy change (ΔH^0) and entropy change (ΔS^0) were calculated and listed in Table S8. In detail, the value of ΔG^0 from −28.19 to −31.3 kJ mol^{-1} implied that the whole adsorption process was spontaneous, which could be ascribed to the physical adsorption and chemical adsorption [52]. The positive ΔH^0 value (16.47 kJ mol^{-1}) of the adsorptive interaction between SS-NH_2-UiO-66-5 and Pb(II) implied the endothermic adsorption process [53]. The ΔS^0 (−155.3 J mol^{-1} K^{-1}) of the adsorption between SS-NH_2-UiO-66-5 and Pb(II) was negative, indicating that the interface tended to be orderly in the adsorption process [54].

The cyclic experiments and the fixed-bed column experiments were adopted directly to evaluate the practicality of SS-NH_2-UiO-66-5 for Pb (II) adsorption. As depicted in Fig. 4d, > 90% removal efficiencies (5.0 mg L^{-1}, sorbent dose = 200.0 mg L^{-1}) can be accomplished within 60.0 min over SS-NH_2-UiO-66-5 after five cycles experiments. Only 20.0 mL HCl solution (pH = 2.0) was utilized to wash the used sorbent within 1.0

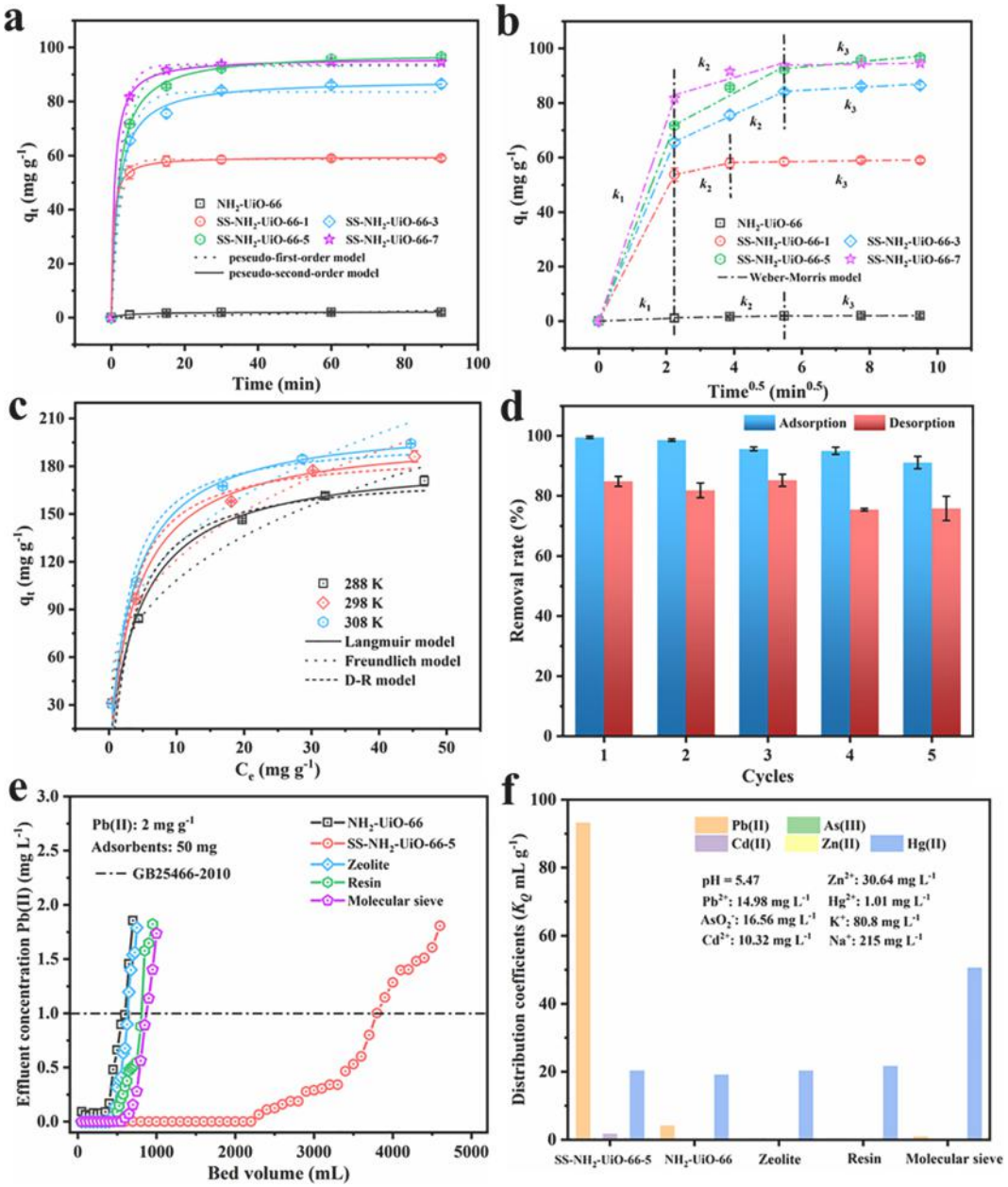

Fig. 4. Pb(II) adsorption (a) kinetic curves and (b) intra-particle diffusion curves (pH = 5.46, T = 25 °C) over NH_2-UiO-66 and SS-NH_2-UiO-66-X, respectively. (c) Lead adsorption isotherms of SS-NH_2-UiO-66-5 under different temperature. (d) Cyclic stability experiments of the SS-NH_2-UiO-66-5, eluent: HCl solution (pH = 2.0), sorbent dosage = 200.0 mg L^{-1}, Pb(II) = 5.0 mg L^{-1}, initial pH = 5.46, T = 25 °C. (e) Breakthrough curves of NH_2-UiO-66, SS-NH_2-UiO-66-5, zeolite, resin, and molecular sieve. (f) The effect of competitive anions for Pb(II) removal over SS-NH_2-UiO-66-5, NH_2-UiO-66, zeolite, resin, and molecular sieve in simulated lead smelting wastewater. Experiments condition: sorbent dose = 200.0 mg L^{-1}, initial pH = 5.47, T = 25 °C.

min of shaking, achieving efficient desorption (> 75%) and regeneration. Meanwhile, the stability of SS-NH_2-UiO-66-5 was further confirmed by PXRD (Fig. 5a), FITR (Fig. 5b) and SEM (Fig. 5c and d). In addition, we selected 1.0 mg L^{-1} as the limiting value (the emission standard of discharge standards for pollutants from lead and zinc industry (GB 25466-2010)). The results of fixed-bed column experiments (Fig. 4e) indicated that the as-prepared SS-NH_2-UiO-66-5 (50.0 mg) could purify 3800 mL simulated Pb(II)-containing wastewater (initial concentration: 2.0 mg L^{-1}), which was higher than those of NH_2-UiO-66 (50.0 mg, 600 mL), zeolite (50.0 mg, 625 mL), resin (50.0 mg, 800 mL) and molecular sieve (50.0 mg, 850 mL) under the identical conditions. Afterwards, these exhausted samples were subjected to in situ desorption by washing with HCl solution (pH = 2.0). As depicted in Fig. S11b, less than 300.0 mL desorption agent was required to wash the SS-NH_2-UiO-66-5, indicating that it possessed potentially excellent preconcentration function toward Pb(II). Furthermore, the Zr dissolution of SS-NH_2-UiO-66-5 during the column tests all keep at a low level (less than 1.16 mg L^{-1}) (Fig. S12). Overall, these results confirmed high adsorption/desorption performance of SS-NH_2-UiO-66-5, indicating that it could be expected for the long-term adsorption applications and even for the sample pretreatment for the real environment simples.

3.3. Mechanism of Pb(II) removal using SS-NH_2-UiO-66-5

After the adsorption of Pb(II), the HR-TEM and the corresponding elemental mapping (Fig. S13) showed the uniform distribution of Pb(II) throughout the used NH_2-UiO-66 and SS-NH_2-UiO-66-5. The results of zeta potential (Fig. S8a) demonstrated the potentials of both SS-NH_2-

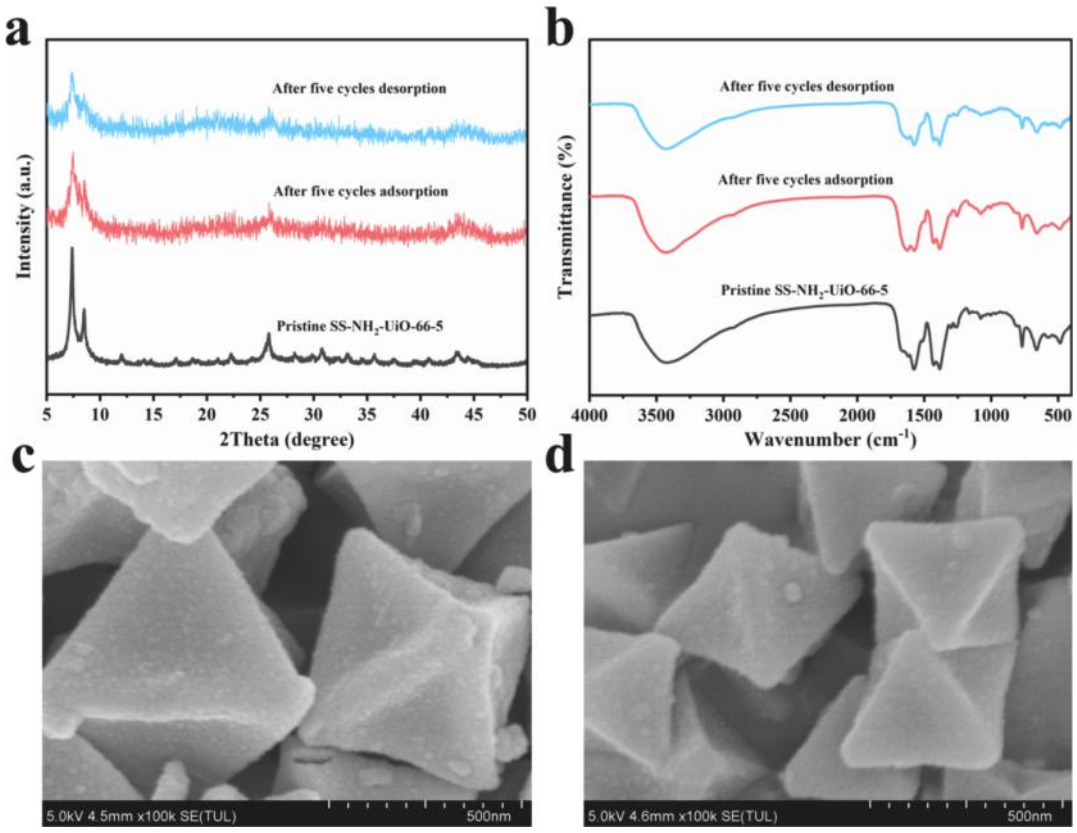

Fig. 5. (a) The PXRD, (b) FTIR spectra of the pristine SS-NH_2-UiO-66-5 and the used one after five cyclic adsorption and desorption experiments. The SEM images of SS-NH_2-UiO-66-5 after five cyclic (c) adsorption and (d) desorption experiments.

UiO-66-5 (-112.9 mV) and NH_2-UiO-66 (−82.8 mV) were negative at pH = 5.46. Thus, electrostatic interaction between Pb(II) and both SS-NH_2-UiO-66-5 and NH_2-UiO-66 contributed primarily to the adsorption process. After the adsorption of Pb(II) by pristine NH_2-UiO-66, the N 1 s spectrum (Fig. S13h) showed that a shift of ca. 0.23 eV to lower binding energy occurred, demonstrating that the –NH_2 functional groups showed high affinity with Pb(II) [48]. After the adsorption of Pb(II) by SS-NH_2-UiO-66-5, the characteristic peak of Pb 4f appeared in the XPS survey scan (Fig. S13c). The peak of Pb 4f could be divided into Pb $4f_{5/2}$ (139.30 eV) and Pb $4f_{7/2}$ (144.12 eV) corresponding to $Pb(OH)_2$ and Pb (II), respectively [55,56], indicating that a chelate form between the N and O on the SS-NH_2-UiO-66-5 with Pb(II). As shown in Fig. S13e, a shift of ca. 0.12 eV to higher binding energy occurred, which could attribute to the formation of Zr-O-Pb [57]. And the N 1 s spectrum (Fig. S13f) showed that a red shift of 0.24 eV happened to the binding energy of –NH after adsorption, demonstrating that the N atoms in the –NH_2 functional groups were chelated with Pb(II) [51,58]. Thus, the results of XPS showed that both Zr-OH and –NH_2 chelated with Pb(II) to achieve the adsorption. The EXAFS spectra (Figs. 6 and S14) displayed that the generation of sorption sites by defect engineering played a significant role during the adsorption process. The XANES spectra demonstrated that the intensity of white line (first resonance after the edge) was decrease after the adsorption process. The intensity decrease of white line may be attributed to the formation of Pb-O bonds on the Zr-O cluster. After the adsorption process, the signals of Zr-Zr/Pb appeared in the EXAFS spectra of SS-NH_2-UiO-66-5(Pb), further affirming that the formation of bond between Pb and uncoordinated oxygen on the Zr-O cluster. Moreover, if the Zr-Zr or Zr-Pb was fixed, the increase of uncertainty further indicated that Zr-Zr and Zr-Pb were presented on the Zr-O cluster. Thus, the appearance of Zr—Pb peak further confirmed there were rich sorption sites in the Zr—O cluster, and the change of intensity and symmetry of the Zr—O peak after adsorption were attributed to the formed Zr—O—Pb bonds.

3.4. DFT calculations

To clarify the influence of missing BDC-NH_2 and Zr vacancies in SS-NH_2-UiO-66-5 toward selective uptake Pb(II), the possible interaction situations between the perfect NH_2-UiO-66/defective SS-NH_2-UiO-66-5, and the various heavy metal ions like Pb(II), Cd(II), Tl(I/III) and Zn(II) were explored at the molecule level with the aid DFT calculations. The sorption energy coordination (N-Pb, MM, mononuclear monodentate) of perfect unit cell NH_2-UiO-66 (Fig. 7a and b) was calculated as −0.971 eV, indicating that the adsorption behavior was a spontaneous process [20]. After modulation with seignette salt, the missing linker and zirconium defects were shown in Fig. 7f, g and k. it was worth noting that the corresponding adsorption energy (N-Pb (MM)) in the missing linker defects was −1.394 eV, which was smaller than that in the perfect unit cell. The results indicated that the formed hierarchical pores in SS-NH_2-UiO-66-5 contributed primarily to the boosting adsorption affinity toward Pb(II) and accelerating the transport of Pb(II) toward sorption active sites. Moreover, apart from the N-Pb (MM) coordination, other sorption pathways were also observed (O-Pb (BB, binuclear bidentate)). The O-Pb interaction displayed that these uncoordinated oxygen atoms (Zr vacancies) due to the missing zirconium on the Zr-O cluster offered another direct combination form toward Pb(II) (Fig. 3b), and the adsorption energy (−1.954 eV) of O-Pb coordination was lower than that of both perfect and defect unit cell. The induced hierarchical pores and vacancy-rich defects by seignette salt formed some adsorption sites, which strengthened the mass transport of Pb(II) within SS-NH_2-UiO-66-5 to shorten the time to achieve the Pb(II) uptake equilibrium. In addition, to affirm the mechanism of selective sorption over SS-NH_2-UiO-66-5 toward Pb(II), the adsorption energies of some adjacent toxic metal ions (Cd(II), Tl(I/III) and Zn(II)) with Pb(II) in periodic table were

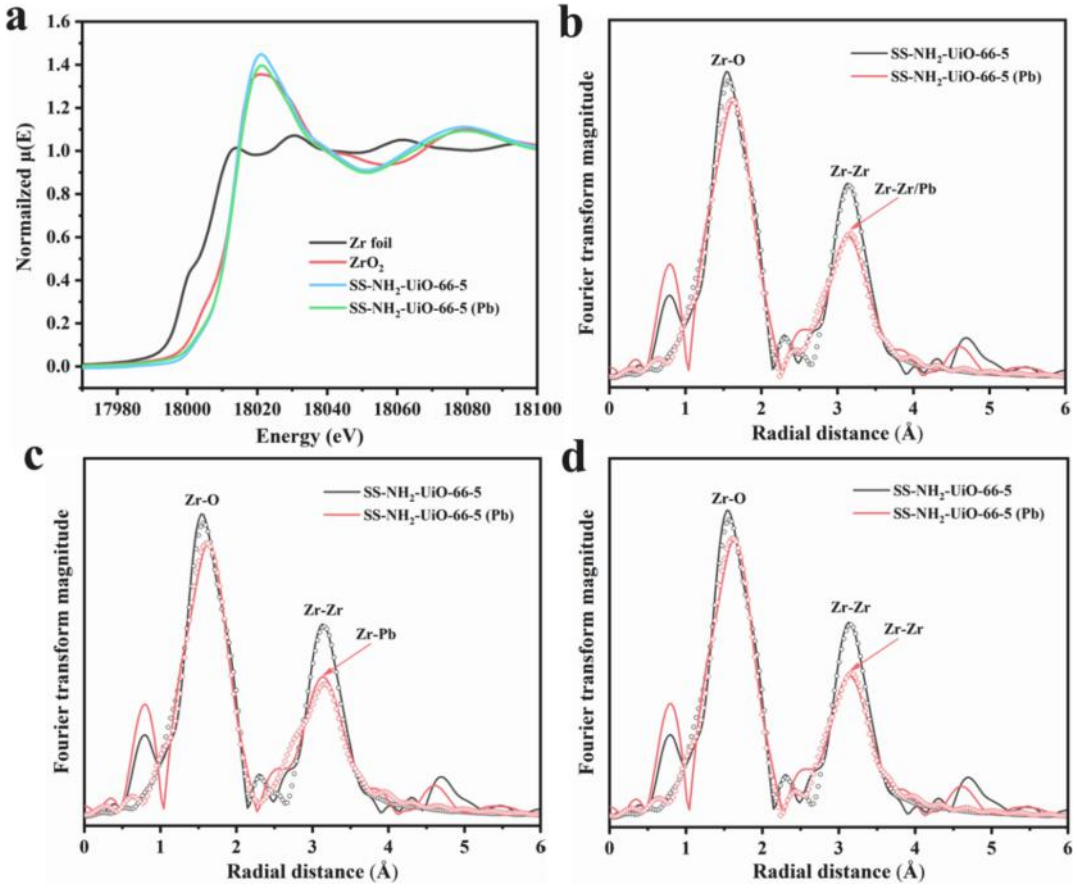

Fig. 6. (a) XANES and (b-d) EXAFS spectra of the Zr K-edge in SS-NH_2-UiO-66-5 and after adsorption (SS-NH_2-UiO-66-5 (Pb)). Experimental and calculated c1urves were displayed as black/red lines and black/red open circles, respectively.

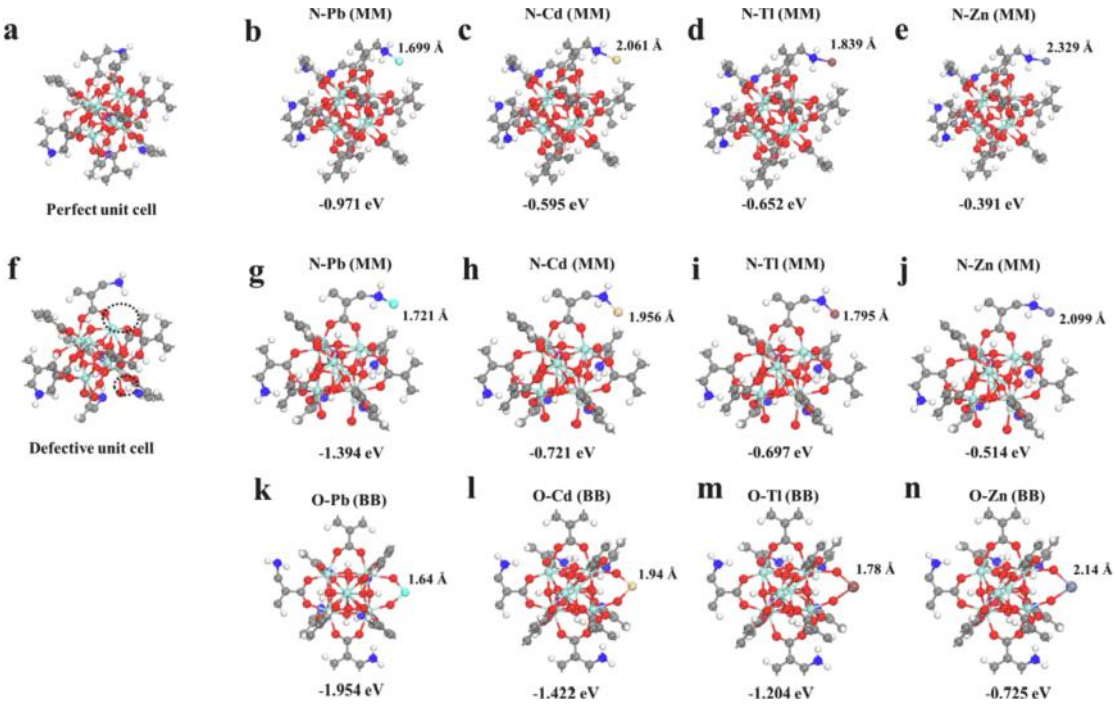

Fig. 7. DFT calculation models for different heavy metal atoms and structures: (a) perfect NH_2-UiO-66 unit cell, (b) N-Pb (MM) (c) N-Cd (MM) (d) N-Tl (MM) (e) N-Zn (MM) coordination between perfect NH_2-UiO-66 and heavy metal pollutants, (f) the defective NH_2-UiO-66 with missing linkers and Zr unit cell, (g) N-Pb (MM) (h) N-Cd (MM) (i) N-Tl (MM) (j) N-Zn (MM), (k) O-Pb (BB), (l) O-Cd (BB), (m) O-Tl (BB), (n) O-Zn (BB) coordination between defective NH_2-UiO-66 and heavy metal pollutants. Cyan for Zr, and red for O from the Zr-O cluster, bule for N from BDC-NH_2.

calculated. SS-NH_2-UiO-66-5 possessed lower adsorption energy toward Pb(II) than those of other metal ions, which was in good agreement with corresponding experiment (Fig. S15). The results of distribution coefficients (K_Q, mL g^{-1}, the details were given in the SI, Section S3) displayed that the binding affinity followed the order Pb(II) (26.43 mL g^{-1}) > Cd(II) (0.85 mL g^{-1}) > Tl(I/III) (0.46 mL g^{-1}) > Zn(II) (0.28 mL g^{-1}). The DFT calculation results were agreed well with the experimental results, affirming the proposed mechanism of selective adsorption of SS-NH_2-UiO-66-5 toward Pb(II).

3.5. Environmental application

The efficiency of sorbents for uptake Pb(II) was easily influenced by pH values in aqueous solution [50]. Moreover, it was expected that the sorbent could keep long-term stability in aqueous solution. Thus, the Pb (II) adsorption and corresponding Zr(Ⅳ) dissolution experiments were performed at pH = 2.01, 3.04, 4.06, 5.02 and 5.46. Some metal complexes (Fig. S8b) like $Pb(OH)_{2aq}$, Pb_2OH^{3+}, $PbOH^+$, $Pb(OH)_3^-$ and so on might be produced in solution with higher pH [59]. Therefore, the optimal pH was explored under acidic conditions. As shown in Fig. S16, the SS-NH_2-UiO-66-5 exhibited the highest Pb(II) adsorption capacity at pH = 5.46. At lower pH, the adsorbent was easily protonated due to the massive H^+ ions, in which the electrostatic repulsion inhibited the adsorption interactions between SS-NH_2-UiO-66-5 and Pb(II) [60]. This pH value was also more in line with the actual pH in the nature environment. In addition, the results of the concentrations of leached-out Zr demonstrated that the zirconium dissolution was 0.24 mg L^{-1} at pH = 5.46, indicating that the adsorbent maintained the outstanding water stability.

To further explore the efficiency of SS-NH_2-UiO-66-5 for Pb(II) removal in practical environments, the effect of adsorption behavior the simulated wastewater formulated by tap water and lake water along with the simulated lead smelting wastewater were examined as well (Tables S11 and S12). As depicted in Figs. S17 and S18, SS-NH_2-UiO-66-5 could remove nearly 100% Pb(II) in the simulated wastewater formulated with real tap and lake water within 60.0 min. Fig. 4f indicated that SS-NH_2-UiO-66-5 displayed good selective adsorption even though there were many other co-existing metal ions in simulated lead smelting wastewater. By contrast, other sorbents showed a weak adsorption ability and selectivity toward Pb(II) in wastewater. Moreover, the distribution coefficients (K_Q, mL g^{-1}) and selectivity coefficients (K, the details were given in the SI, Section S3) were also introduced to check the selective adsorption toward Pb(II) in solution by SS-NH_2-UiO-66-5, NH_2-UiO-66, zeolite, resin, and molecular sieve (Table S14). As to SS-NH_2-UiO-66-5, the K_Q (93.14 mL g^{-1}) value of Pb (II) was larger than other ions like Cd(II), Zn(II), As(III), Hg(II) in the wastewater, demonstrating that the SS-NH_2-UiO-66-5 displayed the strongest adsorption interaction and highest removal rate toward Pb(II). In addition, SS-NH_2-UiO-66-5 displayed larger selectivity coefficient K value for ions matrix in the simulated wastewater [51], indicating that its functional group as well as vacancies formed weak affinity with the co-existing metal ions.

4. Conclusions

In conclusion, a new type of defects had been rationally designed and fabricated using different concentration seignette salt to modulate Zr-MOFs especially NH_2-UiO-66, which was affirmed by XPS, EPR, TGA, EA, XANES and EXAFS. The expansion of pore dimension and increase of adsorption sites vastly boost its adsorption capacity toward Pb(II). Among the as-prepared SS-NH_2-UiO-66-X adsorbents, SS-NH_2-UiO-66-5 demonstrated the best adsorption performance due to the presence of mesopores and macropore, more adsorption sites (unsaturated coordination centers). The maximum adsorption capacity of SS-NH_2-UiO-66-5 reached 186.14 mg g^{-1} at 25 °C and initial pH = 5.46, which was about 34.2 times higher than that of pristine NH_2-UiO-66. Moreover, SS-NH_2-UiO-66-5 displayed excellent Pb(II) selectivity in simulated wastewater (tap lake, lake water and lead smelting wastewater). The XPS and EXAFS results demonstrated that the uncoordinated oxygens on the Zr-O cluster and the N atoms in the –NH_2 functional groups played significant roles for the enhanced Pb(II) adsorption process. The DFT results further illustrated the significant influence of the formed defects in SS-NH_2-UiO-66-X for boosting the adsorption interaction toward Pb(II) by constructing massive active bonding sites and boosting the mass transfer of Pb(II) in SS-NH_2-UiO-66-X framework. Further investigation will be conducted to provide a universal toolkit for modulating tunable porous frameworks with facile synthetic approach for effective pollutants removal.

Declaration of Competing Interest

The authors declare that they have no known competing financial interests or personal relationships that could have appeared to influence the work reported in this paper.

Acknowledgements

This work was supported by National Natural Science Foundation of China (51878023), Beijing Natural Science Foundation (8202016), Great Wall Scholars Training Program Project of Beijing Municipality Universities (CIT&TCD20180323), Beijing Talent Project (2020A27), Science and Technology General Project of Beijing Municipal Education Commission (KM202110016010) and The Fundamental Research Funds for Beijing University of Civil Engineering and Architecture (X20147/X20141/X20135/X20146).

Appendix A. Supplementary data

Supplementary data to this article can be found online at https://doi.org/10.1016/j.cej.2022.136276.

References

[1] C.-C. Wang, J.-R. Li, X.-L. Lv, Y.-Q. Zhang, G. Guo, Photocatalytic organic pollutants degradation in metal-organic frameworks, Energy Environ. Sci. 7 (9) (2014) 2831–2867.
[2] H.C. Zhou, J.R. Long, O.M. Yaghi, Introduction to metal-organic frameworks, Chem. Rev. 112 (2) (2012) 673–674.
[3] B. Li, H.M. Wen, Y. Cui, W. Zhou, G. Qian, B. Chen, Emerging multifunctional metal-organic framework materials, Adv. Mater. 28 (40) (2016) 8819–8860.
[4] X. Du, S. Wang, F. Ye, Z. Qingrui, Derivatives of metal-organic frameworks for heterogeneous fenton-like processes: from preparation to performance and mechanisms in wastewater purification – A mini review, Environ. Res. 206 (2022), 112414.
[5] Y. Li, Y. Xia, K. Liu, K. Ye, Q. Wang, S. Zhang, Y. Huang, H. Liu, Constructing Fe-MOF-derived Z-scheme photocatalysts with enhanced charge transport: nanointerface and carbon sheath synergistic effect, ACS Appl. Mater. Interfaces 12 (22) (2020) 25494–25502.
[6] Y. Bai, Y. Dou, L.H. Xie, W. Rutledge, J.R. Li, H.C. Zhou, Zr-based metal-organic frameworks: design, synthesis, structure, and applications, Chem. Soc. Rev. 45 (8) (2016) 2327–2367.
[7] S. Yuan, J.-S. Qin, C.T. Lollar, H.-C. Zhou, Stable metal-organic frameworks with group 4 metals: current status and trends, ACS Cent. Sci. 4 (4) (2018) 440–450.
[8] X. Zhang, S. Tong, D. Huang, Z. Liu, B. Shao, Q. Liang, T. Wu, Y. Pan, J. Huang, Y. Liu, M. Cheng, M. Chen, Recent advances of Zr based metal organic frameworks photocatalysis: Energy production and environmental remediation, Coord. Chem. Rev. 448 (2021) 214177.
[9] H. Fu, C.-C. Wang, W. Liu, MOFs for Water Purification, Chin. Chem, Lett, 2021.
[10] L. Feng, G.S. Day, K.-Y. Wang, S. Yuan, H.-C. Zhou, Strategies for pore engineering in zirconium metal-organic frameworks, Chemistry 6 (11) (2020) 2902–2923.
[11] S. Yuan, L. Zou, J.S. Qin, J. Li, L. Huang, L. Feng, X. Wang, M. Bosch, A. Alsalme, T. Cagin, H.C. Zhou, Construction of hierarchically porous metal-organic frameworks through linker labilization, Nat. Commun. 8 (2017) 15356.
[12] L. Jiao, J.Y.R. Seow, W.S. Skinner, Z.U. Wang, H.-L. Jiang, Metal–organic frameworks: Structures and functional applications, Mater. Today 27 (2019) 43–68.
[13] A. Kirchon, J. Li, F. Xia, G.S. Day, B. Becker, W. Chen, H.J. Sue, Y. Fang, H.C. Zhou, Modulation versus templating: fine-tuning of hierarchally porous PCN-250 using fatty acids to engineer guest adsorption, Angew. Chem. Int. Ed. Engl. 58 (36) (2019) 12425–12430.

[14] G. Cai, P. Yan, L. Zhang, H.C. Zhou, H.L. Jiang, Metal-organic framework-based hierarchically porous materials: synthesis and applications, Chem. Rev. 121 (20) (2021) 12278–12326.
[15] Z. Chen, S.L. Hanna, L.R. Redfern, D. Alezi, T. Islamoglu, O.K. Farha, Reticular chemistry in the rational synthesis of functional zirconium cluster-based MOFs, Coord. Chem. Rev. 386 (2019) 32–49.
[16] T.C. Wang, W. Bury, D.A. Gomez-Gualdron, N.A. Vermeulen, J.E. Mondloch, P. Deria, K. Zhang, P.Z. Moghadam, A.A. Sarjeant, R.Q. Snurr, J.F. Stoddart, J. T. Hupp, O.K. Farha, Ultrahigh surface area zirconium MOFs and insights into the applicability of the BET theory, J. Am. Chem. Soc. 137 (10) (2015) 3585–3591.
[17] M. Taddei, When defects turn into virtues: the curious case of zirconium-based metal-organic frameworks, Coord. Chem. Rev. 343 (2017) 1–24.
[18] S. Chong, G. Thiele, J. Kim, Excavating hidden adsorption sites in metal-organic frameworks using rational defect engineering, Nat. Commun. 8 (1) (2017) 1539.
[19] L. Feng, K.Y. Wang, X.L. Lv, T.H. Yan, H.C. Zhou, Hierarchically porous metal-organic frameworks: synthetic strategies and applications, Natl. Sci. Rev. 7 (11) (2020) 1743–1758.
[20] M. Li, Y. Liu, F. Li, C. Shen, Y.V. Kaneti, Y. Yamauchi, B. Yuliarto, B. Chen, C.-C. Wang, Defect-rich hierarchical porous UiO-66(Zr) for tunable phosphate removal, Environ. Sci. Technol. 55 (19) (2021) 13209–13218.
[21] G. Cai, X. Ma, M. Kassymova, K. Sun, M. Ding, H.L. Jiang, Large-scale production of hierarchically porous metal-organic frameworks by a reflux-assisted post-synthetic ligand substitution strategy, ACS Cent. Sci. 7 (8) (2021) 1434–1440.
[22] L. Pei, X. Zhao, B. Liu, Z. Li, Y. Wei, Rationally tailoring pore and surface properties of metal-organic frameworks for boosting adsorption of Dy^{3+}, ACS Appl. Mater. Interfaces 13 (39) (2021) 46763–46771.
[23] Y.H. Li, Z. Di, J. Ding, D. Wu, Z. Luan, Y. Zhu, Adsorption thermodynamic, kinetic and desorption studies of Pb^{2+} on carbon nanotubes, Water Res. 39 (4) (2005) 605–609.
[24] J. Luo, M. Sun, C.L. Ritt, X. Liu, Y. Pei, J.C. Crittenden, M. Elimelech, Tuning Pb(II) adsorption from aqueous solutions on ultrathin iron oxychloride (FeOCl) nanosheets, Environ. Sci. Technol. 53 (4) (2019) 2075–2085.
[25] C. Winder, N.G. Carmichael, P.D. Lewis, Effects of chronic low level lead exposure on brain development and function, Trends Neurosci. 5 (1982) 207–209.
[26] J.H. Cavka, S. Jakobsen, U. Olsbye, N. Guillou, C. Lamberti, S. Bordiga, K. P. Lillerud, A new zirconium inorganic building brick forming metal organic frameworks with exceptional stability, J. Am. Chem. Soc. 130 (42) (2008) 13850–13851.
[27] H. Furukawa, F. Gandara, Y.B. Zhang, J. Jiang, W.L. Queen, M.R. Hudson, O. M. Yaghi, Water adsorption in porous metal-organic frameworks and related materials, J. Am. Chem. Soc. 136 (11) (2014) 4369–4381.
[28] E. Lemaire, R. Moser, C.J. Borsa, D. Briand, Green paper-based piezoelectronics for sensors and actuators, Sens. Actuat. A Phys. 244 (2016) 285–291.
[29] K.K. Tripathi, D. Banerjea, Nicotinamidoxime as an analytical reagent, Fresenius Z. Anal. Chem. 176 (2) (1960) 91–96.
[30] G. Wißmann, A. Schaate, S. Lilienthal, I. Bremer, A.M. Schneider, P. Behrens, Modulated synthesis of Zr-fumarate MOF, Microporous Mesoporous Mater. 152 (2012) 64–70.
[31] Y.-H. Li, X.-H. Yi, Y.-X. Li, C.-C. Wang, P. Wang, C. Zhao, W. Zheng, Robust Cr(VI) reduction over hydroxyl modified UiO-66 photocatalyst constructed from mixed ligands: performances and mechanism insight with or without tartaric acid, Environ. Res. 201 (2021), 111596.
[32] J. Guo, X. Fan, J. Wang, S. Yu, M. Laipan, X. Ren, C. Zhang, L. Zhang, Y. Li, Highly efficient and selective recovery of Au(III) from aqueous solution by bisthiourea immobilized UiO-66-NH_2: performance and mechanisms, Chem. Eng. J. 425 (2021), 130588.
[33] L. Hao, X. Li, M.J. Hurlock, X. Tu, Q. Zhang, Hierarchically porous UiO-66: facile synthesis, characterization and application, Chem. Commun. 54 (83) (2018) 11817–11820.
[34] Q. He, Q. Chen, M. Lü, X. Liu, Adsorption Behavior of Rhodamine B on UiO-66, Chin. J. Chem. Eng. 22 (11–12) (2014) 1285–1290.
[35] S. Sadeghi, M. Jafarzadeh, A. Reza Abbasi, K. Daasbjerg, Incorporation of CuO NPs into modified UiO-66-NH_2 metal-organic frameworks (MOFs) with melamine for catalytic C-O coupling in the Ullmann condensation, New J. Chem. 41 (20) (2017) 12014–12027.
[36] G.C. Shearer, S. Chavan, J. Ethiraj, J.G. Vitillo, S. Svelle, U. Olsbye, C. Lamberti, S. Bordiga, K.P. Lillerud, Tuned to perfection: ironing out the defects in metal-organic framework UiO-66, Chem. Mater. 26 (14) (2014) 4068–4071.
[37] S. Zhang, Y. Zhuo, C.I. Ezugwu, C.C. Wang, C. Li, S. Liu, Synergetic molecular oxygen activation and catalytic oxidation of formaldehyde over defective MIL-88B (Fe) nanorods at room temperature, Environ. Sci. Technol. 55 (12) (2021) 8341–8350.
[38] M. Kandiah, M.H. Nilsen, S. Usseglio, S. Jakobsen, U. Olsbye, M. Tilset, C. Larabi, E.A. Quadrelli, F. Bonino, K.P. Lillerud, Synthesis and stability of tagged UiO-66 Zr-MOFs, Chem. Mater. 22 (24) (2010) 6632–6640.
[39] L. Valenzano, B. Civalleri, S. Chavan, S. Bordiga, M.H. Nilsen, S. Jakobsen, K. P. Lillerud, C. Lamberti, Disclosing the complex structure of UiO-66 metal organic framework: a synergic combination of experiment and theory, Chem. Mater. 23 (7) (2011) 1700–1718.
[40] D. Liu, D. Chen, N. Li, Q. Xu, H. Li, J. He, J. Lu, Surface engineering of g-C_3N_4 by stacked BiOBr sheets rich in oxygen vacancies for boosting photocatalytic performance, Angew. Chem. Int. Ed. Engl. 59 (11) (2020) 4519–4524.
[41] K. Ye, K. Li, Y. Lu, Z. Guo, N. Ni, H. Liu, Y. Huang, H. Ji, P. Wang, An overview of advanced methods for the characterization of oxygen vacancies in materials, Trends, Analyt. Chem. 116 (2019) 102–108.
[42] G. Ye, H. Wang, X. Zeng, L. Wang, J. Wang, Defect-rich bimetallic UiO-66(Hf-Zr): Solvent-free rapid synthesis and robust ambient-temperature oxidative desulfurization performance, Appl. Catal. B: Environ. 299 (2021), 120659.
[43] R. Xu, Q. Ji, P. Zhao, M. Jian, C. Xiang, C. Hu, G. Zhang, C. Tang, R. Liu, X. Zhang, J. Qu, Hierarchically porous UiO-66 with tunable mesopores and oxygen vacancies for enhanced arsenic removal, J. Mater. Chem. A 8 (16) (2020) 7870–7879.
[44] F. Meng, S. Zhang, L. Ma, W. Zhang, M. Li, T. Wu, H. Li, T. Zhang, X. Lu, F. Huo, J. Lu, Construction of hierarchically porous Nanoparticles@Metal-Organic frameworks composites by inherent defects for the enhancement of catalytic efficiency, Adv. Mater. 30 (49) (2018) e1803263.
[45] Y.S. Ho, G. McKay, Pseudo-second order model for sorption processes, Process Biochem. 34 (5) (1999) 451–465.
[46] J. Sagiv, Organized monolayers by adsorption. 1. Formation and structure of oleophobic mixed monolayers on solid surfaces, J. Am. Chem. Soc. 102 (1) (1980) 92–98.
[47] D. Liu, Z. Li, Y. Zhu, Z. Li, R. Kumar, Recycled chitosan nanofibril as an effective Cu (II), Pb(II) and Cd(II) ionic chelating agent: adsorption and desorption performance, Carbohydr. Polym. 111 (2014) 469–476.
[48] Y. Liu, J. Xu, Z. Cao, R. Fu, C. Zhou, Z. Wang, X. Xu, Adsorption behavior and mechanism of Pb(II) and complex Cu(II) species by biowaste-derived char with amino functionalization, J. Colloid. Interface. Sci. 559 (2020) 215–225.
[49] G. Issabayeva, M.K. Aroua, N.M. Sulaiman, Removal of lead from aqueous solutions on palm shell activated carbon, Bioresour. Technol. 97 (18) (2006) 2350–2355.
[50] L. Fu, S. Wang, G. Lin, L. Zhang, Q. Liu, H. Zhou, C. Kang, S. Wan, H. Li, S. Wen, Post-modification of UiO-66-NH_2 by resorcyl aldehyde for selective removal of Pb (II) in aqueous media, J. Clean. Prod. 229 (2019) 470–479.
[51] J. Tang, Y. Chen, M. Zhao, S. Wang, L. Zhang, Phenylthiosemicarbazide-functionalized UiO-66-NH_2 as highly efficient adsorbent for the selective removal of lead from aqueous solutions, J. Hazard. Mater. 413 (2021), 125278.
[52] S. Simsek, Z.M. Senol, H.I. Ulusoy, Synthesis and characterization of a composite polymeric material including chelating agent for adsorption of uranyl ions, J. Hazard. Mater. 338 (2017) 437–446.
[53] A.A. Alqadami, M. Naushad, Z.A. Alothman, A.A. Ghfar, Novel metal-organic framework (MOF) based composite material for the sequestration of U(VI) and Th (IV) metal ions from aqueous environment, ACS Appl. Mater. Interfaces 9 (41) (2017) 36026–36037.
[54] S. Jamshidifard, S. Koushkbaghi, S. Hosseini, S. Rezaei, A. Karamipour, A. Jafari Rad, M. Irani, Incorporation of UiO-66-NH_2 MOF into the PAN/chitosan nanofibers for adsorption and membrane filtration of Pb(II), Cd(II) and Cr(VI) ions from aqueous solutions, J. Hazard. Mater. 368 (2019) 10–20.
[55] N. Hao, J. Cao, J. Ye, C. Zhang, C. Li, B. Bate, Content and morphology of lead remediated by activated carbon and biochar: a spectral induced polarization study, J. Hazard. Mater. 411 (2021), 124605.
[56] J. Zhao, C. Wang, S. Wang, Y. Zhou, Experimental and DFT study of selective adsorption mechanisms of Pb(II) by UiO-66-NH_2 modified with 1,8-dihydroxyanthraquinone, J. Ind. Eng. Chem. 83 (2020) 111–122.
[57] P.-H. Li, Y.-X. Li, S.-H. Chen, S.-S. Li, M. Jiang, Z. Guo, J.-H. Liu, X.-J. Huang, M. Yang, Sensitive and interference-free electrochemical determination of Pb(II) in wastewater using porous Ce-Zr oxide nanospheres, Sens. Actuat. B Chem. 257 (2018) 1009–1020.
[58] J. Zhong, J. Zhou, M. Xiao, J. Liu, J. Shen, J. Liu, S. Ren, Design and syntheses of functionalized copper-based MOFs and its adsorption behavior for Pb(II), Chin. Chem. Lett. 33 (2) (2022) 973–978.
[59] H. Li, S. Mu, X. Weng, Y. Zhao, S. Song, Rutile flotation with Pb^{2+} ions as activator: adsorption of Pb^{2+} at rutile/water interface, Colloid Surface A 506 (2016) 431–437.
[60] J. Ge, J. Xiao, L. Liu, L. Qiu, X. Jiang, Facile microwave-assisted production of Fe_3O_4 decorated porous melamine-based covalent organic framework for highly selective removal of Hg^{2+}, J. Porous Mater. 23 (3) (2016) 791–800.